

RESEARCH ARTICLE

Litchi-derived platinum group metal-free electrocatalysts for oxygen reduction reaction and hydrogen evolution reaction in alkaline media

Seyed Ariana Mirshokraee¹ | Mohsin Muhyuddin¹ | Roberto Lorenzi¹ |
 Giorgio Tseberlidis¹  | Carmelo Lo Vecchio² | Vincenzo Baglio² |
 Enrico Berretti³  | Alessandro Lavacchi³ | Carlo Santoro¹ 

¹Department of Materials Science, University of Milano-Bicocca, Milano, Italy

²Istituto di Tecnologie Avanzate per l'Energia "Nicola Giordano" (ITAE), Consiglio Nazionale delle Ricerche (CNR), Via Salita S., Messina, Italy

³Istituto di Chimica Dei Composti OrganoMetallici (ICCOM), Consiglio Nazionale Delle Ricerche (CNR), Sesto Fiorentino, Firenze, Italy

Correspondence

Carlo Santoro, Department of Materials Science, University of Milano-Bicocca, U5, Via Cozzi 5, 20125, Milano, Italy.
 Email: carlo.santoro@unimib.it

Funding information

Italian Ministry of Education; Universities and Research; Ministero dell'Istruzione, dell'Università e della Ricerca—MIUR, Grant/Award Number: PGR18MAZLI; Italian ministry MIUR; AMPERE, Grant/Award Number: FISR2019_01294

Abstract

Within the framework of the circular economy, the waste litchi's skins were upgraded and transformed into electrocatalysts for oxygen reduction reaction (ORR) and hydrogen evolution reaction (HER). The waste litchi's skins were pyrolyzed, activated, and then used as carbon support for fabricating metal–nitrogen–carbons (M–N–Cs) which belong to a promising class of platinum group metal-free electrocatalysts. The activated char was functionalized with transition metal (Fe, Ni, and Co)- phthalocyanine (Pc) in monometallic and bimetallic fashion by subjecting it to a thermal treatment at 600 and 900°C. The samples functionalized at 900°C showed higher performance for HER due to the formation of metal nanoparticles, whereas the samples functionalized at 600°C showed higher performance for ORR. Particularly, sample Ni–Co 900 had an overpotential of -0.38 V for HER, while the sample Fe 600 was the most active electrocatalyst for ORR by demonstrating the onset potential of ~ 0.9 V (a half-wave potential of ~ 0.81 V) with the least production of unwanted peroxide anion.

KEYWORDS

circular economy, hydrogen evolution reaction, oxygen reduction reaction, PGM-free electrocatalyst

1 | INTRODUCTION

One of the most serious problems for human life and the environment these days is the greenhouse effect and abnormal climate. A huge amount of greenhouse gases is released into the atmosphere by the overuse of fossil and

nonrenewable fuels, such as coal, gas, and oil causing a violent upsurge in the global carbon footprint. As a result, the loss of carbon balance in nature is leading to severe damage to the ecosystem. This global issue is calling for a paradigm shift in the way energy is produced, stored, and used. A suitable option is the utilization of hydrogen

This is an open access article under the terms of the [Creative Commons Attribution](https://creativecommons.org/licenses/by/4.0/) License, which permits use, distribution and reproduction in any medium, provided the original work is properly cited.

© 2023 The Authors. *SusMat* published by Sichuan University and John Wiley & Sons Australia, Ltd.

as an energy vector. This fuel contains gravimetric chemical energy up to 142 MJ kg⁻¹, which is nearly three times higher than fossil fuels or other chemical fuels.¹ Hydrogen as an energy vector with low environmental impact will have a crucial role within the global decarbonization plan set for 2050.² Among different methods for producing hydrogen, the only real green and sustainable method to satisfy the global demand is water electrolysis, powered by renewable energy sources.^{3–5} Following the green route, the utilization of H₂ gas as an efficient fuel for producing electricity can occur in electrochemical devices named fuel cells. Fuel cells can harvest electrical energy from the chemical reaction of fuel (hydrogen) and oxygen, while water is produced as an environmentally-safe byproduct. Fuel cells offer high-energy conversion efficiencies at practically negligible carbon release, which can potentially reduce the discrepancies between environmental concerns and growing energy demands.⁶

However, there are major setbacks that prevent the widespread applications of water electrolyzers and fuel cells. Particularly, slow kinetics and significant overpotentials offered by the cathode side reactions, that is, hydrogen evolution reaction (HER) and oxygen reduction reaction (ORR) in electrolyzers and fuel cells, respectively, are the main restrictions in large-scale implementation of both technologies, as these aforementioned electrochemical reactions have a significant influence on the overall performance.^{7–9} Therefore, great research effort is focused on the improvement of the efficiency of both cathodic reactions. Until now, noble metal-based materials, represented by platinum (Pt), are still the most effective electrocatalysts with very small overpotentials.¹⁰ Nevertheless, noble metals or platinum-group metals (PGMs) are rare, expensive and are considered critical raw materials by the EU.¹¹ Therefore, over the past few decades, a huge scientific interest has been witnessed to limit the usage PGMs and replace them with earth-abundant nonprecious (named also as PGM-free) electrocatalysts.¹²

In such a situation, atomically dispersed first-row transition metals coordinated with nitrogen and embedded in a carbon matrix (M–N–Cs, where M is Fe, Co, Mn, etc.) are emerging as a reliable substitutes, capturing the attention of the scientific community.^{13–18} Some of these types of electrocatalysts have been upscaled to near commercial levels¹⁹, demonstrating reasonable kinetic activity and stability under less corrosive alkaline conditions.^{16,20–22} Carbon is one of the most suitable support materials for all types of electrocatalysts due to its electronic conductivity, stability, cost-efficiency, and flexible structure. The carbon matrix has a defect-rich structure and this property guarantees a conducive platform for the electrocatalytic performance.^{23,24} On the other hand, the transition metals coordinated with nitrogen over the carbon matrix generate

the electrochemically active sites.²⁵ It is worth mentioning that iron coordinated with nitrogen (Fe–N_x with *x* as 2, 3, and 4) is a well-known active site responsible for improving ORR activity.^{16,26,27} Recently, the synthesis of Fe–phthalocyanines (Pc) supported over different carbon matrixes was studied being an attractive iron source owing to: a) its bulky conjugated molecular structure, b) the ability to donate electrons, c) characteristics centrosymmetric arrangement and d) its ability to be a simultaneous source of nitrogen.^{28–30} Meanwhile, Ni–N_x active sites and Ni nanoparticles play an important role in the enhancement of the HER electrocatalysis performance.^{31,32} The stable Ni–N_x sigma bond in the NiPc electrocatalyst is responsible for the efficient evolution of hydrogen.³³ It is noteworthy that, Ni belongs to the 10th group of the periodic table and therefore shares very similar electronic structures with Pd and Pt which are very effective electrocatalysts for the evolution of hydrogen. Importantly also Ni–Fe complexes have shown important electroactivity toward HER by bio-mimicking dehydrogenase enzymes in nature.³⁴

In general, cathode electrocatalysts in both fuel cells and water electrolyzers are based on active sites integrated into the carbon skeleton, where the latter generally corresponds to 90%–99% of the entire electrocatalyst composition. The carbon backbone can be obtained by different precursors other than the one derived from petrochemical processes and in consequence can be derived from cleaner and cost-effective pathways. In recent studies, important development and progress in the synthesis of PGM-free electrocatalysts derived by controlled pyrolysis processes of carbonaceous waste for the electrocatalysis paradigm can be observed.^{35–38} This process has the goal to valorize the waste carbon-containing sources and to transform them into conductive and high surface area char that can serve as valuable carbon backbone for ORR and HER electrocatalysts. After functionalizing the biochar with a proper metal–nitrogen source and integrating the active sites into the carbonaceous skeleton, the obtained powder can be used as an efficient electrocatalyst. With this method, the waste is transformed into a valuable product that improves the resource recycling economy. Recently, researches report the advancements done in this direction for the synthesis of HER and ORR electrocatalysts.^{24,39,40} Different sorts of biochar have been made from different wastes, such as algae, pistachio waste, and tea waste.^{39,41,42} Generally, biochars have chemical stability, optimum electrical conductivity, and considerable mass transportability. Moreover, due to their large surface area and good conductivity, they show high-power charge–discharge potential and high reversible capacity.^{43,44}

Herein, litchi's skin was used as a carbon precursor to produce valuable char. Litchi is a tropical to subtropical fruit with a white gelatinous aril surrounded by a bright

red pericarp and it is cultivated in more than 20 countries around the world. China and India are the first and second producers of litchi, respectively. The worldwide litchi production is between 2.6 and 2.8 million tons.⁴⁵ Litchi pulp is a good source of minerals, such as potassium, calcium, magnesium, manganese, zinc, iron, and even copper.⁴⁶ Moreover, studies have revealed the fact that anthocyanins are responsible for the bright red color.⁴⁷

In this study, the valuable, carbon-rich biochar produced by blended, dried, and pyrolyzed litchi's skins, was used as PGM-free ORR and HER electrocatalyst in an alkaline environment after proper functionalization. The char was activated with KOH and then functionalized through pyrolysis processes by adding the 30 wt% phthalocyanines (Pc) of the metal of interest (FePc, NiPc, and CoPc). Moreover, the mix of these metal phthalocyanines (bimetallic) was used in this project (15 wt% FePc—15 wt% CoPc, 15 wt% FePc—15 wt% NiPc, and 15 wt% NiPc—15 wt% CoPc). The functionalizations were done under controlled pyrolysis with two different temperatures of 600 and 900°C. The obtained electrocatalysts were tested in alkaline electrolytes for the ORR and HER. The effects of synthesis conditions on the overall electrochemical performance in the alkaline conditions were closely analyzed. The results are promising a new possibility of recycling the waste, and a possible replacement of PGM-based electrocatalysts for HER and ORR.

2 | RESULT AND DISCUSSION

2.1 | Characterization of litchi electrocatalysts

A series of microscopic and spectroscopic techniques were used to characterize the surface chemistry and morphology of the synthesized electrocatalysts. Figure 1 reports the comparison of the high-resolution transmission electron microscopy (HRTEM) images of the iron samples functionalized at 600 and 900°C (Fe 600 and Fe 900). Images clearly show that at 600°C no iron or iron oxide nanoparticles are present in the sample (Figure 1A), whereas at 900°C nanoparticles are evident (Figure 1B). This is confirmed by the observation with the STEM HAADF detector. EDX mapping revealed that in the sample pyrolyzed at 600°C iron is evenly distributed on the carbon support (Figure 1A). In the sample functionalized at 900°C iron occurs mainly in the form of nanoparticles. A comparison of the Fe K_{α} and the O K_{α} maps reveals a superimposition of iron and oxygen indicating that the nanoparticles consist of iron oxides.

Figure 2 shows the morphology of the Ni-Co samples functionalized at 600 and 900°C (Ni-Co 600 and

Ni-Co 900). Conversely to the case of iron, the HRTEM investigation showed the presence of nanoparticles even at 600°C (Figure 2A), a finding that was confirmed by the HAADF investigation. Remarkably, the compositional maps obtained by EDX revealed that the Ni and Co signals superimpose in the particle region (Figure 2A). The O and C K maps (Figure 2A) show no superimposition with the Ni and Co patterns, indicating that the nanoparticles consist of metallic alloys of Ni and Co. However, a careful examination of the maps still shows the presence of cobalt and nickel diffused background in the carbon support; this observation suggest that not all the metallic centers introduced in the sample have been converted to nanoparticles. At 900°C (Figure 2B) the HRTEM images show again the presence of nanoparticles. The EDX maps analysis of the nanoparticles is in-line with the analysis of the sample functionalized at 600°C. However, a close look at the Co and Ni maps reveals that the signals of the two metals are not detectable outside the particles in the 900°C sample; accordingly, we could conclude that the conversion of the metallic centers into nanoparticles is complete.

Figure 3 shows the Raman spectra of the functionalized samples, with a focus on two prominent carbon peaks at ca. 1350 and ca. 1588 cm^{-1} , namely, the G- and D band, respectively. Usually, the G band represents the vibrational mode of the movement in opposite directions of two carbon atoms in a graphite sheet. So G band is related to the E_{2g} vibrational mode of sp^2 bonded carbon atoms in graphene sheets where the D band emerges due to breathing modes with A_{1g} symmetry.⁴⁸ The D band is attributed to the defects and disorders in the carbon materials and it is attributable to imperfections in sp^2 carbon structures. In general, the D and D* (which can be seen for Co 600 and Ni-Co 600 samples at about 1600 cm^{-1}) bands are defect-induced Raman features, and thus these bands cannot be seen for highly crystalline graphite.^{49–53} The D* band characteristically emerges due to intravalley double resonance scattering, in which the defect-related discontinuities offer the lost momentum needed to satisfy the resonant process.^{53–56} Where the graphitization is considered favorable for the electron transfer during electrocatalysis, defects and discontinuities within carbonaceous structure act as electro-catalytically active moieties for ORR and can also contribute to HER.^{25,39,57,58,59,60} The intensity ratio I_D/I_G of the D and G band is widely used for characterizing the defect quantity in graphitic materials.

With a comparison between functionalized samples at 600 and 900°C, it can be simply observed that all the peaks in 600°C samples Raman spectra reduced to two main peaks of D and G in 900°C samples. By increasing the functionalized temperature from 600 to 900°C, the intensity ratio I_D/I_G was reduced for the Fe-Co sample and remained at the same level for Fe samples. However, for

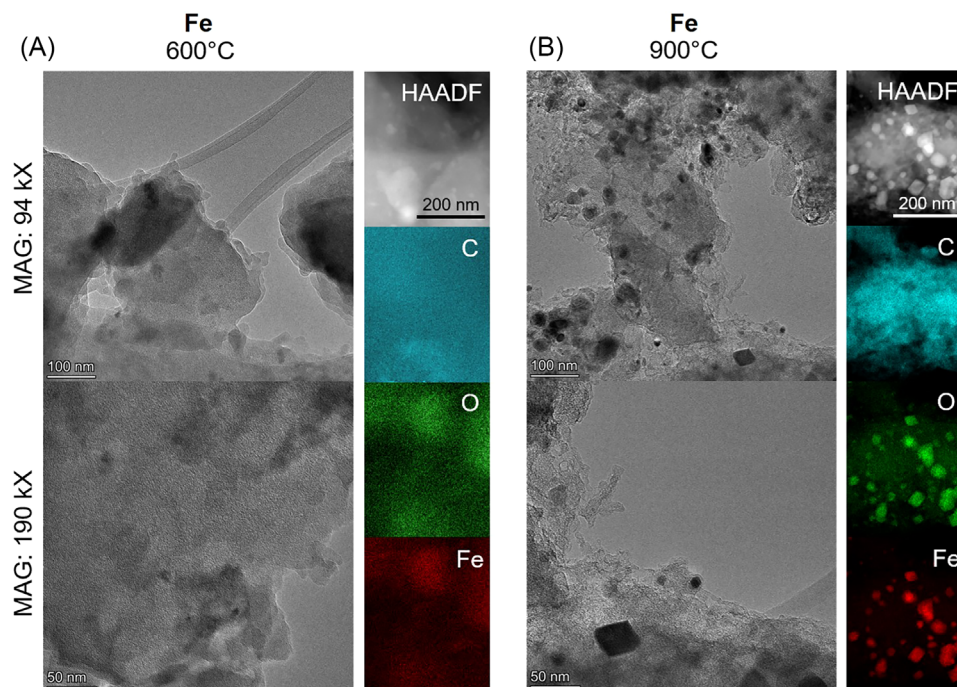


FIGURE 1 (A) High-resolution transmission electron microscopy (HRTEM), HAADF, and EDX maps at the C, O, and Fe K X-ray K of the Fe sample functionalized at 600°C (Fe 600) and (B) HRTEM, HAADF, and EDX maps at the C, O, and Fe X-ray K emissions of the sample functionalized at 900°C (Fe 900).

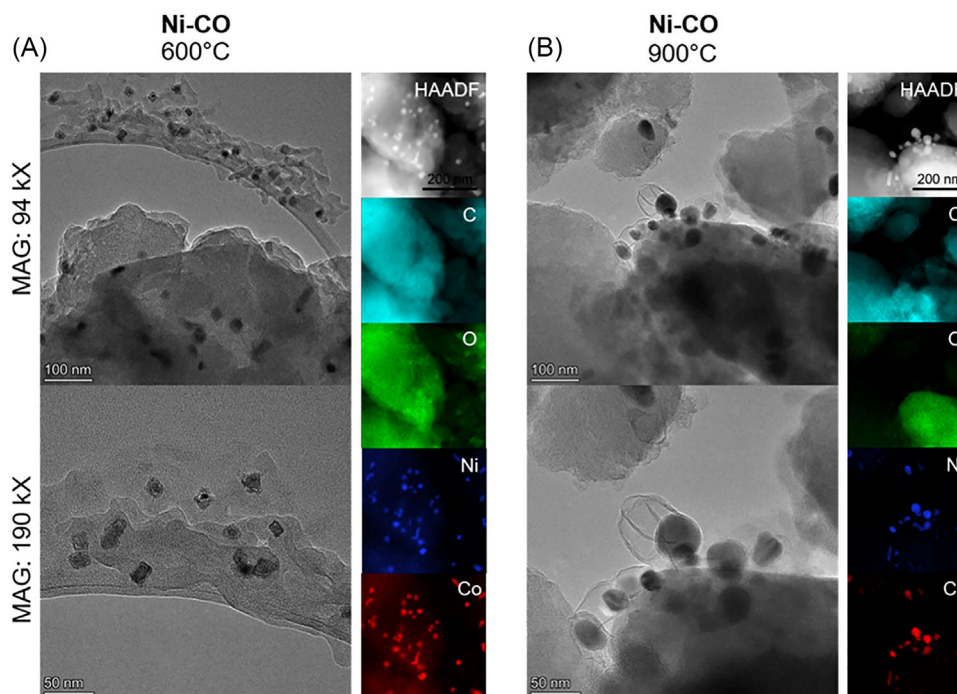


FIGURE 2 (A) High-resolution transmission electron microscopy (HRTEM), HAADF, and EDX maps at the C, O, Co, and Ni X-ray K emissions of the Ni-Co sample functionalized at 600°C (Ni-Co 600) and (B) HRTEM, HAADF, and EDX maps at the C, O, Co, and Ni K X-ray K emissions of the sample functionalized at 900°C (Ni-Co 900).

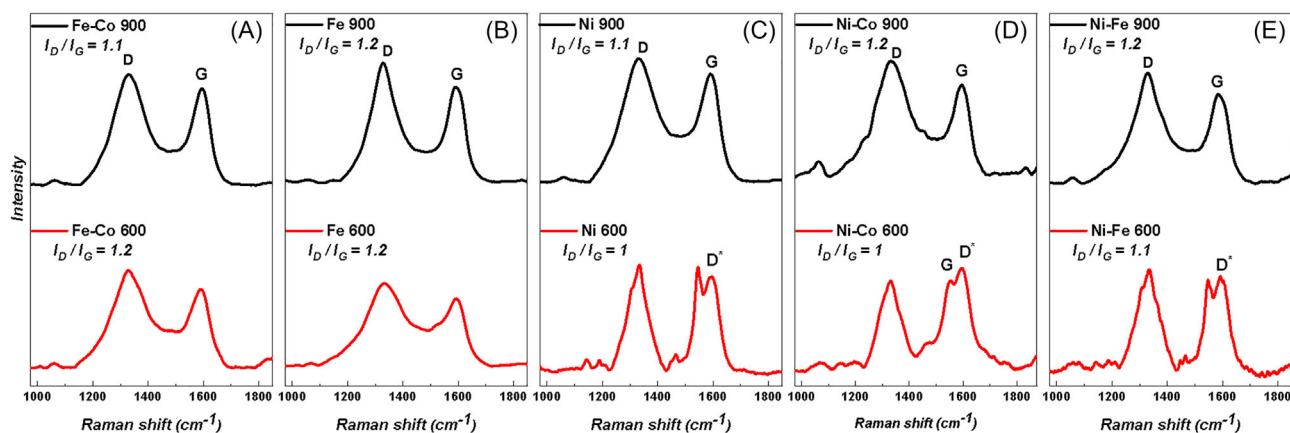


FIGURE 3 Raman spectra of litchi-derived electrocatalysts with two different functionalization temperatures of 900 and 600°C for: (A) Fe-Co, (B) Fe, (C) Ni, (D) Ni-Co, and (E) Ni-Fe samples.

the samples which include Ni, at 600°C mode, the D* peak emerged. The existence of the D* band specifies the occurrence of a large number of different defects, such as destructive grain boundaries and edges, in-plane heteroatom substitution, and atomic vacancies.^{54–56,61,62} By comparing the samples containing Ni, with two functionalization temperatures, it can be observed that the G peak intensity increases and overwhelm the D* peaks when goes from 600 to 900°C. In these samples, contrary to Fe and Fe-Co, the intensity ratio I_D/I_G increases proportionally with the increase of the functionalization temperatures. These outcomes may explain why samples containing Ni have better performance for HER.

To study the crystal structure and phases present, X-ray diffraction (XRD) measurements were launched and the achieved diffraction patterns are demonstrated in Figure 4. At first, the results show the presence of two broad peaks centering nearly at 24° and 44° which belong to the amorphous carbon.⁶³ The samples functionalized at 600°C during the functionalization step mainly showed the broader peaks belonging to carbon (Figure 4A–D,F), whereas the samples functionalized at 900°C additionally showed a few peaks related to metallic species present inside the as-synthesized electrocatalysts. It confirmed that some metal clusters were formed when the metal precursor was functionalized at 900°C. At such temperatures, the metal atoms have sufficient mobility to aggregate into small clusters and nanoparticles.^{64,65} However, in Figure 4E, where the XRD patterns of Ni-Co bimetallic samples are presented, there are Fe peaks related to the metallic phase of Ni and Co in Ni-Co 600 XRD patterns. It confirmed the results that were reported in the HRTEM and Raman analysis, that is, the existence of metallic nanoparticles for Ni-Co samples even with 600°C functionalization temperature.

X-ray photoelectron spectroscopy (XPS) data were interpreted by analyzing the results obtained in the

literature.^{66–73} The survey spectra of Fe, Fe-Co, Ni-Co, and Ni-Fe-based electrocatalysts, treated at 600 or 900°C, are shown in (Figure S1A–C) chiefly indicating the presence of carbon, nitrogen, oxygen, and metals. The unmarked peaks at 315 and 560 eV are related to the shake-up lines of C1s and N1s signals, respectively, whereas the other tiny and narrow peaks between C1s and N1s regions correspond to a low amount (<0.3%) of potassium and calcium, mainly addressed to litchi residuals. C1s is the predominant species in all the compounds with the atomic percentage of about 80% for the catalysts treated at 600°C and about 90% for the catalysts treated at 900°C, as reported in (Table S1). Furthermore, the electrocatalysts treated at 600°C display atomic percentages of N1s (10.8% for Fe 600) and metals (Fe or Co) larger than that achieved for the electrocatalysts treated at 900°C.

XPS spectra for N1s signals are shown in (Figure 5A–C). As reported in the literature,^{66,67,69,72} the deconvolution can be obtained by considering six different N-species for the Fe–N–C catalyst: imine (397.5 ± 0.1 eV), pyridinic-N (398.2 ± 0.1 eV), N_x-Fe (399.5 ± 0.1 eV), pyrrolic-N (400.8 ± 0.1 eV), graphitic-N (402.1 ± 0.1 eV), and oxidized nitrogen species (>403 eV). The deconvoluted spectra for Fe–Co–N–C were gathered considering pyridinic-N (398.2 ± 0.2 eV), N_x-Fe (399.1 ± 0.1 eV), pyrrolic-N (400.1 ± 0.1 eV), graphitic-N (401.1 ± 0.1 eV), and oxidized nitrogen signals (>402.5 eV), as reported in the previous study concerning Fe–Co embedded in nitrogen and carbonaceous species.^{68–71} For bimetallic Ni–Co 900 and Ni–Fe 900, a deconvoluted fit was acquired by keeping constant binding energy (BE) values of a Fe–N–C electrocatalyst to extract the BE value of the N–M interaction. A BE value of 399.0 ± 0.1 eV was achieved corresponding to the same value reported in a few papers in the literature.⁷⁴ By comparing the results in Figure 5A and summarized in Table S2, the amount of pyridinic-N species, for the

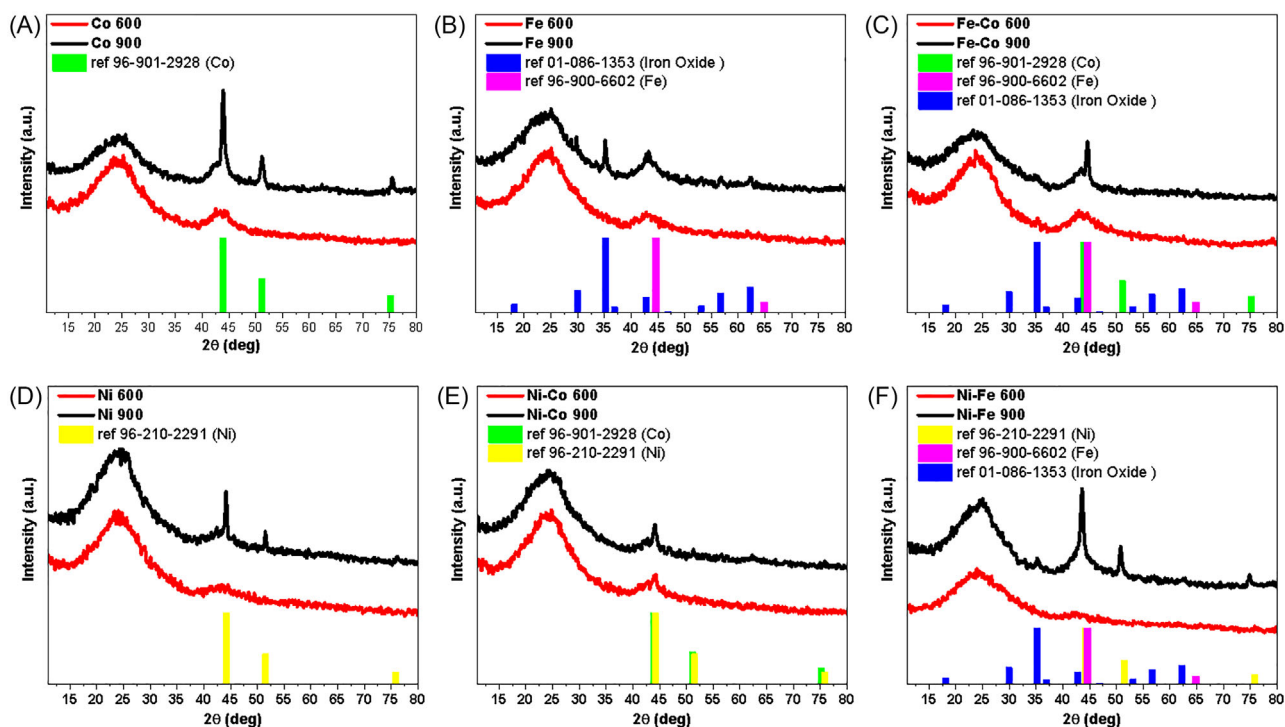


FIGURE 4 X-ray diffraction (XRD) spectra of litchi electrocatalysts with two different functionalization temperatures of 900 and 600 °C for: (A) Co, (B) Fe, (C) Fe–Co, (D) Ni, (E) Ni–Co, and (F) Ni–Fe samples.

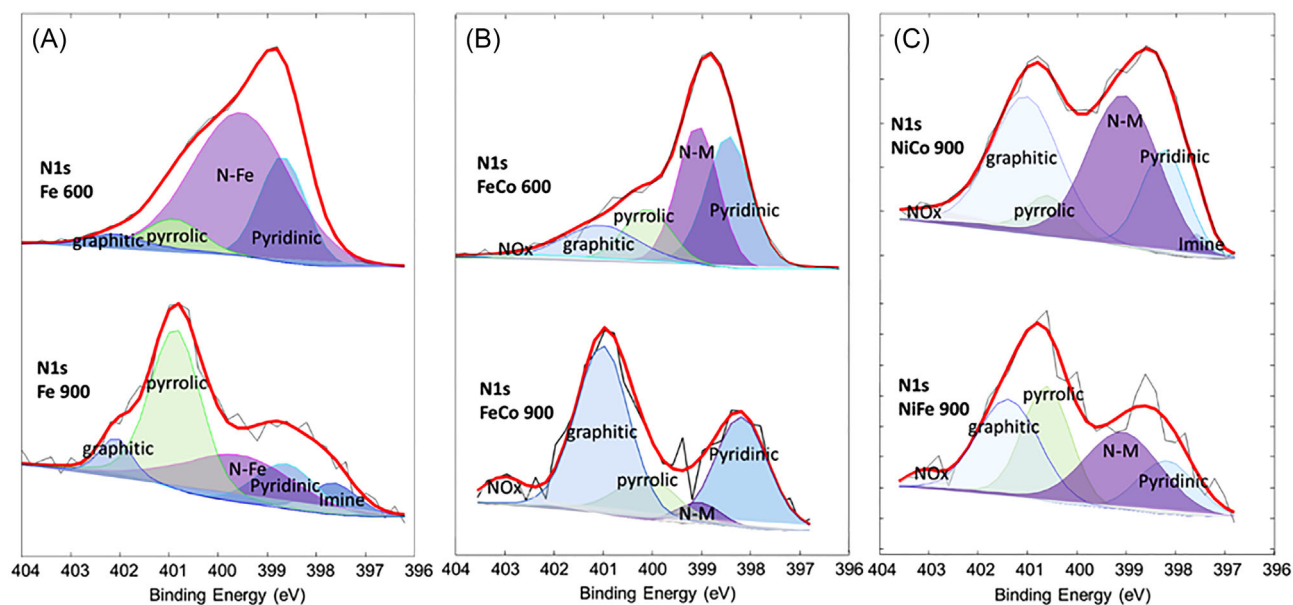


FIGURE 5 Comparison of X-ray photoelectron spectroscopy (XPS) N1s signal for: (A) Fe 600 and Fe 900, (B) Fe–Co 600 and Fe–Co 900, and (C) Ni–Co 900 and Ni–Fe 900.

Fe 600 catalyst, is larger than that achieved for Fe 900, and the content of pyrrolic-N species increases with the electrocatalyst treated at a higher temperature. The same decrease of pyridinic species is achieved for FeCo-based electrocatalysts with the higher temperature treatment

(Figure 5B) whereas, in this case, there is a clear increase of graphitic-N moieties instead of pyrrolic-N. As described in the literature, in an acid environment N-pyrrolic species generate a major production of H_2O_2 in the ORR process and a decrease in the overall activity.⁶⁷ On the other hand,

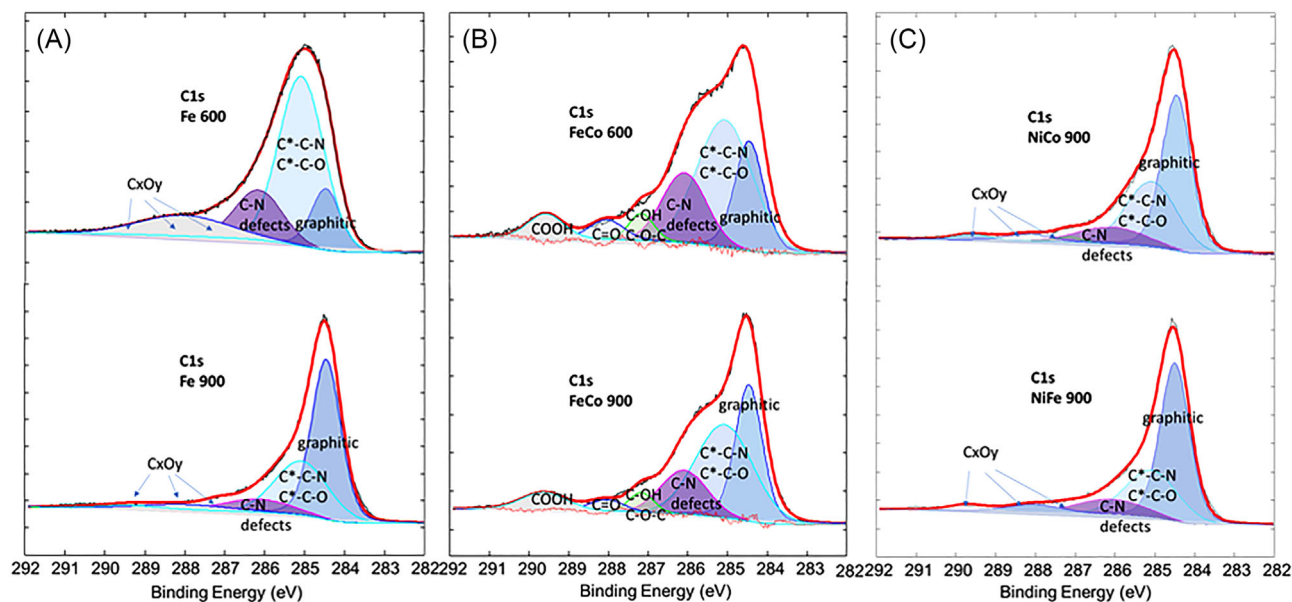


FIGURE 6 Comparison of X-ray photoelectron spectroscopy (XPS) C1s signal for: (A) Fe 600 and Fe 900, (B) Fe–Co 600 and Fe–Co 900, and (C) Ni–Co 900 and Ni–Fe 900.

pyridinic and graphitic nitrogen contribute to a higher ORR activity. In an alkaline environment, there is not a direct correlation between nitrogen moieties and ORR activity for the different electron transfer reaction mechanism that is mainly promoted by the presence of hydroxyl groups over the electrocatalyst surface.^{75,76} The most important data, reported in Figure 5A–C and in Table S2, is the strong interaction between N and metal atoms for Fe 600 (66.3%) and Fe–Co 600 (33.0%). The relative percentage of this interaction is drastically reduced for the catalysts treated at 900°C, probably due to the decomposition of nitrogen species at high temperatures and to a lower overall N atomic percentage (Tables S1 and S2) over the surface of Fe 900 and Fe–Co 900. Among the catalysts treated at a higher temperature, Ni–Co 900 has shown the largest N–M interactions (37.67%), followed by Ni–Fe 900 (28.51%).

Peaks such as graphitic carbon (284.4 eV), secondary carbons due to the coordination of carbon such as carbon-nitrogen and/or carbon-oxides (285 eV), CN_x defects (286.2 eV), C–OH/C–OC (287.1 eV), C=O (288 eV), and COOH (289.4 eV) are fitted in the high-resolution C1s spectra and shown in (Figure 6A–C). The relative percentage of each species is reported in (Table S3). Fe 600 and Fe–Co 600 are characterized by a lower relative amount of graphitic carbon and by a larger relative percentage of C– N_x defects compared to Fe 900 and Fe–Co 900. For Ni–Co 900 and Ni–Fe 900, the relative percentages of the components are following those achieved for the catalysts treated at 900°C with a large contribution of graphitic carbon (>49%) and a mean value of C–N defects (about 11%).

2.2 | Electrochemical performance

For testing HER and ORR, the char obtained from litchi was activated, mixed with metal phthalocyanines, and finally functionalized via pyrolysis at two different temperatures of 600 and 900°C. All the electrocatalysts were tested in alkaline media for both the reactions. 1 M KOH was used as alkaline electrolyte for HER measurement. Particularly for HER, the samples Char, Active Char, and different functionalized M–N–C were tested and compared. Moreover, the same samples were tested for ORR in 0.1 M KOH as their electrolyte.

2.2.1 | Hydrogen evolution reaction (HER) performance

The obtained electrocatalysts were then analyzed for HER. Linear sweep voltammetry (LSV) was performed in the 0 to -0.9 V potential range vs. reversible hydrogen electrode (RHE) in alkaline media (Figure 7). The measurements were acquired at a scan rate of 5 mV s^{-1} with 1600 rpm of rotating disk speed. The overpotentials were calculated at the current density of -10 mA cm^{-2} according to the literature.⁵ By first looking at the result, it can be observed that litchi's char showed the lowest HER activity among all the samples tested. The activation of the litchi's char enhanced its performance with the overpotential of -0.8 ± 0.01 V; however, it was far from being acceptable. The overpotentials were further reduced, and

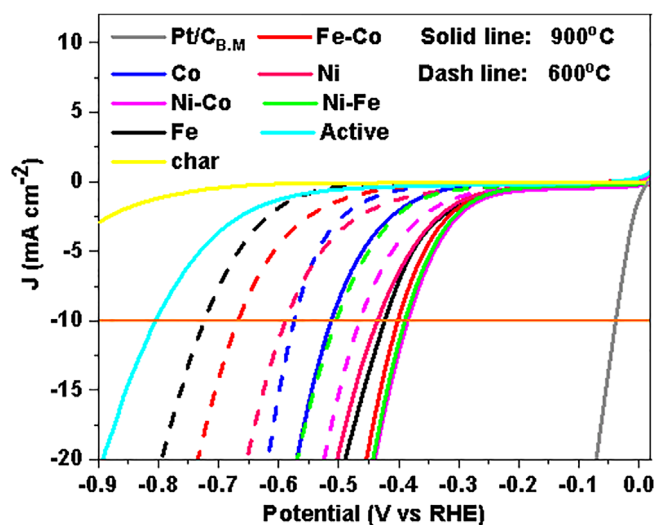


FIGURE 7 The linear sweep voltammetry (LSVs) of rotating disk electrode (RDE) measurement on litchi's samples. B.M in Pt/C_{B.M} means benchmark.

the HER reaction activity was increased after the functionalization of the electrocatalysts with the transition metals (Table S4). In general, the LSV results demonstrate that electrocatalysts with a functionalization temperature of 900°C have higher performance compared to those functionalized at 600°C, probably due to the formation of metal nanoparticles that favor the HER.⁷⁷

The addition of the second transition metal in a bimetallic fashion also improved the electrocatalytic activity by reducing the overpotentials. The bimetallic electrocatalysts containing Ni–Co, Ni–Fe, and Fe–Co, functionalized at 900°C, have the best electrocatalytic activity toward HER with the overpotential of $-0.38 \text{ V} \pm 0.01 \text{ V}$, $-0.39 \text{ V} \pm 0.01 \text{ V}$, and $-0.40 \text{ V} \pm 0.01 \text{ V}$, respectively. Moreover, the samples treated at 600°C that have a bimetallic structure such as Ni–Co and Ni–Fe showed higher HER activity than Ni 600 which is a monometallic sample. The HER measurements clearly show that the functionalized samples derived from combining two different metal–Pcs have higher electroactivity toward the evolution of H₂, especially, those combinations that contain NiPc.

Moreover, one of the crucial properties of electrocatalysts, especially the ones that are made from waste products, is their operative stability. To test HER stability on Ni–Co 900, an accelerated stability test was used.^{78,79} In this measurement, 2000 voltammetric cycles with the scan rate of 50 mV s^{-1} were executed. Meanwhile, the polarization curves at the first cycle and after every 500 cycles were measured with a 5 mV s^{-1} scan rate; the scans are reported in (Figure S2). The first major change in the measured overpotential at 10 mA cm^{-2} occurred within the first 500 cycles (it dropped from $-0.38 \text{ V} \pm 0.01 \text{ V}$ to -0.40

$\text{V} \pm 0.01 \text{ V}$). The activity remained the same from the 500th cycle to the 1500th cycle. But, another major drop happened within the final 500 cycles and the overpotential changed from $-0.40 \text{ V} \pm 0.01 \text{ V}$ to $-0.43 \text{ V} \pm 0.01 \text{ V}$.

In this work, by combining the two metals in bimetallic samples, and controlling the temperatures of thermal treatments during the synthesis, the performances of the monometallic electrocatalysts containing Fe and Ni for HER were improved (Table S6). However, even after improvement, the electrocatalyst which was synthesized from the waste of litchi fruits is still not comparable with Pt/C, but will be subject to further research in the future due to all its promising features.

2.2.2 | Oxygen reduction reaction (ORR) performance

The ORR activities of the activated char and the functionalized samples were measured by performing rotating ring disk electrode (RRDE) measurements at 1600 rpm in oxygen-saturated 0.1 M KOH. The results are shown in (Figure 8). In these measurements, a loading of 0.6 mg cm^{-2} electrocatalyst was deposited for each sample over the disk. The onset potentials for ORR were calculated at the current density of -0.1 mA cm^{-2} which is a benchmark value utilized for identifying the overpotentials of ORR. According to the achieved results, the functionalized char with Fe and Co at 600°C (Fe–Co 600) demonstrated the maximum onset potential at $\sim 0.9 \text{ V}$ versus RHE.

The half-wave potential ($E_{1/2}$), which is related to the reaction kinetics, was estimated using the first differential method (Table S5). The Fe–Co 600 sample shows the both highest onset potential (E_{on}) and half-wave potential ($E_{1/2}$) with 0.9 V (vs. RHE) at 0.1 mA cm^{-2} and 0.81 V of $E_{1/2}$, respectively. Thus, it was the electrocatalyst showing the highest electrocatalytic activity toward ORR among the litchi-derived samples. Besides (Fe–Co 600) which is a bimetallic Fe-containing sample, (Fe 600) as a monometallic M–N_x–C type electrocatalyst showed similar electrocatalytic activity resulting in 0.89 V (vs. RHE) at 0.1 mA cm^{-2} as E_{on} and 0.81 V (vs. RHE) of $E_{1/2}$. Ni samples displayed very low performance in both 600 and 900°C functionalization temperatures. The ring current measured during the LSV is reported in (Figure 8C,D). By considering the ring and disk current, the peroxide anion-produced percent and the number of electron transfers were calculated.

From the kinetic point of view, acceptable electrocatalysts that drive the ORR activity should have higher operating potentials and lower intermediate peroxide anion species production.³⁶ Figure 8G,H displays the peroxide anion-produced yield for the litchi-derived

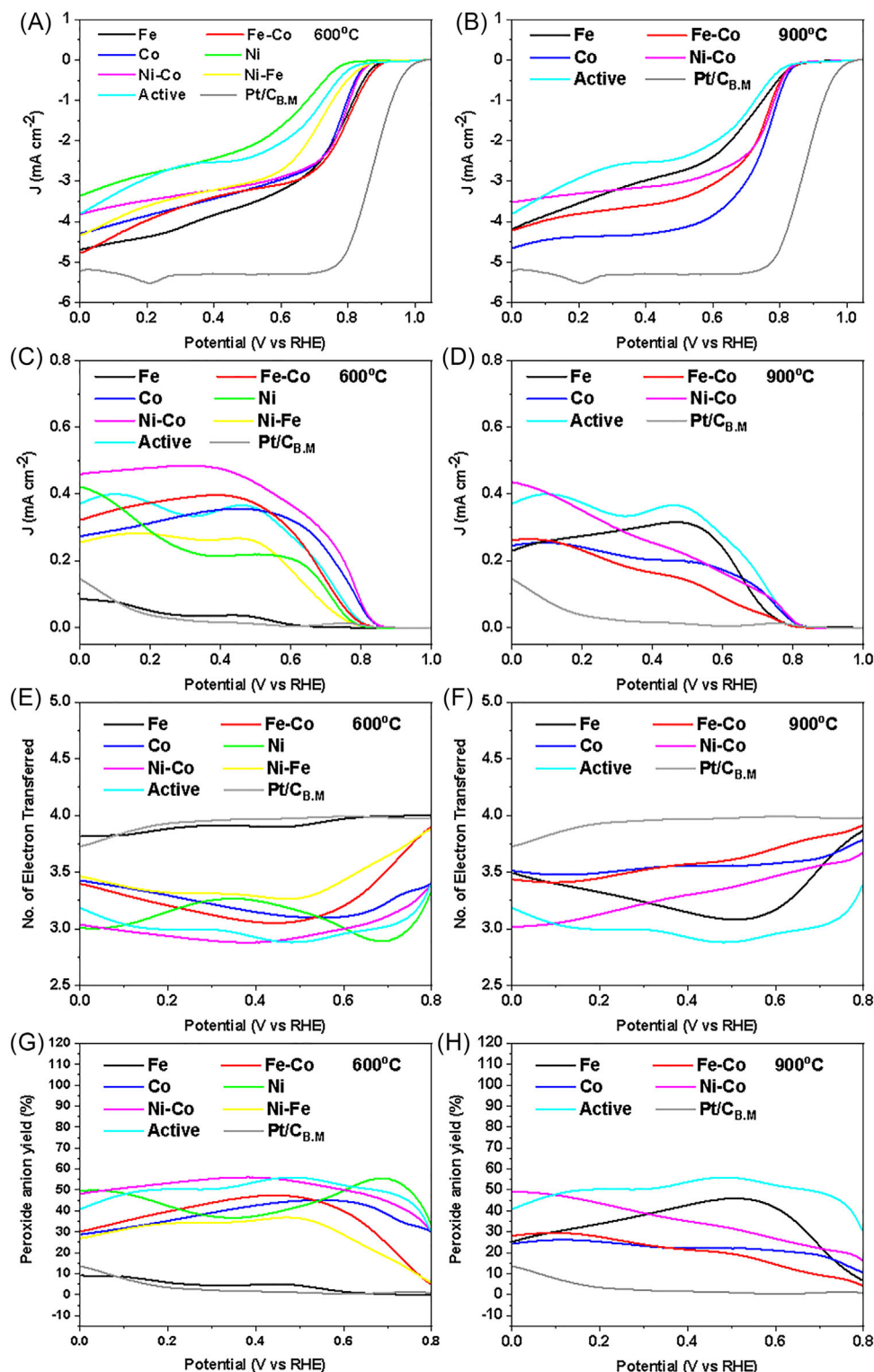


FIGURE 8 The rotating ring disk electrode (RRDE) measurements for oxygen reduction reaction (ORR) running at 1600 rpm. (A) Linear sweep voltammetry (LSV) at 600°C, (B) LSV at 900°C, (C) ring current at 600°C (D) ring current at 900°C, (E) number of electrons transferred at 600°C, (F) number of electrons transferred at 900°C, (G) peroxide anion yield at 600°C, and (H) peroxide anion yield at 900°C. B.M in Pt/C_{B.M} means benchmark.

samples. Importantly, it can be observed that the Fe sample with 600°C temperature treatment produces less peroxide anion compared to 900°C samples. Fe 600 displayed the lowest peroxide anion production, that is, a maximum ca. 10%. The efficient ORR with low peroxide anion produced by the Fe-N_x-C electrocatalyst agrees with the existing literature.^{42,80–83} Interestingly, Co 900 produced slightly less peroxide anion compared to Co 900. Moreover, it can be noticed that except for the Fe 600, there is not much difference between monometallic and bimetallic samples in terms of peroxide anion production.⁸⁴ Moreover, due to the highest electrocatalytic activity and the lowest peroxide anion produced, Fe 600 exhibited the highest number of electron transfers with more than 3.5. The other samples, independently from the functionalization temperature or type of TM contained in the electrocatalysts, show electron transformation between 3 and 3.5. Figure 8E,F reports the number of electron transfers for each sample during RRDE measurement. Samples containing Fe showed the highest ORR performance. On the other hand, the Ni-contained samples, especially Ni 600, showed inferior performance. The complete results are exhibited in Table S5.

One of the interesting aspects to be highlighted is the difference between E_{on} and $E_{1/2}$ in the functionalized samples at a temperature of 600°C with those ones at 900°C. In fact, in general, the 600°C samples have lower overpotentials compared to the samples at 900°C. An explanation might be related to the presence and abundance of nanoparticles. In fact, as it was demonstrated in the structure and chemical characterization section, the functionalization done at 900°C led to the formation of a larger quantity of nanoparticles compared to 600°C where, in the function of the TMs, lower or no nanoparticles were formed and single atom TMs coordinated with nitrogen active sites were predominantly formed. Therefore, M-N_x-C active sites are more desired compared to the nanoparticles for ORR.

Related to the stability test for ORR, 2000 cycles accelerated stability test was performed over Fe 600 sample, whereas the potential window and electrolytic conditions remained as before.^{78,79} As it was mentioned in the previous section, in this study, continuous potential cycling was conducted at a rate of 50 mV s⁻¹, whereas initial and every 500th scans were recorded at a rate of 5 mV s⁻¹ and their results are shown in (Figure S3). The E_{on} and $E_{1/2}$ did not show significant change over the continuous potential cycling, but by increasing the cycle number the reduction in the limiting current density could be observed. As the cycles proceeded, the ring current density shot up. Moreover, the peroxide anion yield which is related to the disk current and the ring current results showed an enhancement. By comparing the 2000th cycle to the 1st cycle, it can be seen that peroxide anion yield got increased three times. Meanwhile, with the same comparison but for the num-

ber of electrons transferred, it experienced a reduction in number, from 3.8 to 3.5.

According to the ORR electrochemical measurements results, Fe 600 demonstrated considerable performance. This electrocatalyst exhibited a similar E_{on} and $E_{1/2}$ as the M-N-Cs electrocatalysts previously investigated (Table S7). In addition, not only it shows remarkable results for the number of electrons transferred and producing the peroxide anion which is comparable with Pt/C, but also, it showed acceptable durability in alkaline media.

3 | CONCLUSIONS

In this work, a costworthy biochar was derived from litchi's skin for the synthesis of a M-N-C electrocatalyst. During the char production, the micro-macroporous architecture was formed, and the surface area of the carbon char was increased by KOH activation. The final electrocatalyst was synthesized by mixing the activated char with the required metal-Pc. The mixtures were successfully functionalized at two different temperatures of 600 and 900°C. The HER and ORR performance of the achieved samples were studied electrochemically in alkaline media.

The first comparison was done between two groups of samples with different functionalized temperatures. Generally, the samples functionalized at 900°C showed higher electrocatalytic activity toward HER. This might be due to the formation of metal nanoparticles that favor the HER as demonstrated by HRTEM and XRD characterization. On the other hand, the 600°C samples performed better for the ORR, due to the absence of metal nanoparticles, and the presence of atomically dispersed active sites.

The second comparison comes to the different metal combinations in the samples. For the HER measurement, Ni-Co 900 which is a bimetallic electrocatalyst had the best performance with the overpotential of -0.38 ± 0.01 V. In the ORR case, although Fe 600 had a similar onset potential (~ 0.9 V vs. RHE) and half-wave potential (~ 0.81 V vs. RHE) with Fe-Co 600 but it produced significantly lower peroxide anion during its activity. Thus, Fe 600 demonstrated the overall most suitable characteristics to be used as a PGM-free electrocatalyst for ORR.

4 | MATERIALS AND METHODS

4.1 | Materials

Litchi's skins were initially recovered and dried at 85°C for 72 h to remove all the moisture. All the chemicals and reagents used to carry out the current study were of analytical grade and were used without any further

processing. Potassium hydroxide (KOH, 99.0% purity), ethanol ($\text{CH}_3\text{CH}_2\text{OH}$), acetone ($(\text{CH}_3)_2\text{CO}$), Nafion 5 wt% hydroalcoholic solution, iron(II) phthalocyanine ($\text{C}_{32}\text{H}_{16}\text{N}_8\text{Fe}$, herein after named Fe-Pc), Nickel(II) phthalocyanine ($\text{C}_{32}\text{H}_{16}\text{N}_8\text{Ni}$, herein after named Ni-Pc), and Cobalt(II) phthalocyanine ($\text{C}_{32}\text{H}_{16}\text{CoN}_8$, herein after named Co-Pc) were purchased from Acros Organics. Nitrogen, oxygen, and argon gases used in this study possess ultrahigh purity features. Ultrapure deionized water obtained from a Millipore Milli-Q system (resistivity $>18 \text{ M}\Omega \text{ cm}$) was used for the experiments.

4.2 | Electrocatalyst synthesis

Fully dried skins were ground to a powder using a coffee blender. The obtained powder was placed into a ceramic boat and inserted into a horizontal tubular furnace with a controlled atmosphere (UHP Ar at $100 \text{ cm}^3 \text{ min}^{-1}$). For the first pyrolysis, the temperature was increased with a heating rate of 5°C min^{-1} to reach 900°C . After remaining at the selected temperature for 1 h, the temperature was decreased with a ramp of 5°C min^{-1} until the room temperature was achieved. The yield for the output/input weight of the first pyrolysis was $\sim 25\%$.

After the first pyrolysis, for enhancing the surface area and creating M-N_x active sites on the surface, the obtained char was first activated and then functionalized. In the first step, the char was impregnated with KOH solution (in 30 mL ethanol). The adjusted mass ratio of the KOH/char was 4.⁸⁵ Then, the solution was stirred for 12 h.⁸⁶ The mixture was dried in an Ar environment at 80°C under continuous stirring. The obtained sludge was then subjected to a heat treatment (second pyrolysis) at 700°C while keeping the dwell time at 1 h in a tube furnace under the controlled atmosphere (UHP Ar at $100 \text{ cm}^3 \text{ min}^{-1}$). The heating rate for increasing and decreasing temperature before and after the dwell was 5°C min^{-1} . The activated char was then washed with 1 M HCl and plenty of Milli-Q water (until a neutral pH was achieved) as soon as it was recovered from the oven, followed by drying in a vacuum oven at 80°C for 12 h. The yield for the output/input weight of the activation was $\sim 50\%$.

The activated char was homogeneously mixed with the metal phthalocyanine of choice (FePc, NiPc, and CoPc) by using a high-energy ball-miller (E_{max} Retsch) for 1 h with one consecutive cooling break of 5 min after 30 min at the rotation rate of 400 rpm. The final functionalization (third pyrolysis) was performed on the mixed samples with two different temperatures of 600 and 900°C in the controlled atmosphere (UHP Ar at $100 \text{ cm}^3 \text{ min}^{-1}$). Moreover, in this pyrolysis, the heating rate of increasing and decreasing temperature before and after dwell time was 5°C min^{-1}

as previously reported.⁸⁷ Table 1 shows the samples that were synthesized and tested in this work.

4.3 | Characterizations

HRTEM images were taken with a Thermo-fisher Talos F200X G2 at an acceleration voltage of 200 kV with a camera resolution of 4096×4096 pixels without any objective apertures. HAADF images were taken with an annular STEM detector with a convergent beam with an angle of 10.5 mrad. EDX maps were collected with a Super X spectrometer equipped with four 30 mm^2 silicon drift detectors for a collection angle of 0.7 srad. A helium-neon laser with an excitation wavelength of 632.8 nm is used for Raman spectroscopy (Jobin Yvon, France). A microscope (BX40, Olympus, Japan) fitted with a $50\times$ long-working-distance objective (0.6 N.A.) focused the laser on the sample, whereas a silicon CCD was used for signal collection (Sincerity, Jobin Yvon, France). XRD (Rigaku Miniflex 600) of powder samples was employed with the copper source. The performed angle range was 10° – 90° with a step of 0.020° , whereas the scanning speed was $1.000^\circ/\text{min}$.

A Physical Electronics (PHI) 5800-01 spectrometer was employed to investigate the surface characteristics of the catalysts within XPS, using a monochromatic Al K_α X-ray source at a power of 350 W, as reported in our previous papers.^{66,68}

4.4 | Electrochemical testing

4.4.1 | Hydrogen evolution reaction

The HER was studied with the three-electrode method with the rotating disk electrode (RDE) technique. The cell was equipped with a glassy carbon disk as a working electrode (glassy carbon with a geometric area of 0.1963 cm^2), which was mounted on a RDE equipment (Pine WaveVortex RDE system coupled with a Pine bipotentiostat) and had a rotation speed of 1600 rpm, a saturated calomel electrode (SCE) as a reference electrode, and a Pt wire as the counter electrode. The inks were prepared by mixing (5 mg) of electrocatalyst with $985 \mu\text{L}$ of isopropanol and $15 \mu\text{L}$ of 5 wt% Nafion D-520 ionomer solution as reported previously.⁷⁸ For each measurement, 0.6 mg cm^{-2} ink was deposited over GC disk. HER was performed in an alkaline media containing 1 M KOH. The benchmark Pt electrocatalyst used in this study was 20 wt% Pt supported on carbon (Pt/C), with a loading of $30 \mu\text{g Pt cm}^{-2}$ on RDE.⁸⁸ To remove residual oxygen from the electrolyte solution for HER measurement and avoid unwanted reactivity, the nitrogen gas was kept flushing into the solution for 15 min

TABLE 1 Name of the electrocatalysts studied and the synthesis steps done.

Sample	First pyrolysis	Activation	Mix with metal-Pc			Functionalization	
			Fe Pc (wt%)	Ni Pc (wt%)	Co Pc (wt%)	600°C	900°C
Char	✓						
Active-char	✓	✓					
Fe 600	✓	✓	30			✓	
Fe 900	✓	✓	30				✓
Ni 600	✓	✓		30		✓	
Ni 900	✓	✓		30			✓
Co 600	✓	✓			30	✓	
Co 900	✓	✓			30		✓
Ni-Co 600	✓	✓		15	15	✓	
Ni-Co 900	✓	✓		15	15		✓
Ni-Fe 600	✓	✓	15	15		✓	
Ni-Fe 900	✓	✓	15	15			✓
Fe-Co 600	✓	✓	15		15	✓	
Fe-Co 900	✓	✓	15		15		✓

before running the measurement. All measured potentials were corrected and converted to potential versus RHE according to the following equation:

$$E_{\text{RHE}} = E_{\text{ref}} + 0.059 \cdot \text{pH} + E_{\text{ref}}^0 \quad (1)$$

where E_{ref} is the measured working potential versus the reference electrode, E_{ref}^0 is the potential of the reference electrode with respect to the standard hydrogen electrode at 25°C (0.241 V for SCE). The potential scan range was maintained from 0 to −0.9 V versus RHE in alkaline media, whereas the overpotential of each electrocatalyst was evaluated at the current density of 10 mA cm^{−2}.

4.4.2 | Oxygen reduction reaction

Three-electrode system comprising a RRDE was used to study the ORR electrochemical activity of the samples. The cell was assembled with an RRDE (Pine WaveVortex RDE system coupled with a Pine bipotentiostat) as a working electrode (the geometric area of the glassy carbon disk was 0.2376 cm² and the platinum ring had a geometric area of 0.2356 cm²). The experiments were performed using a rotation speed of 1600 rpm. An SCE was immersed into the solution and used as a reference electrode. The counter electrode was a graphite rod. The inks were prepared as described above and deposited over the glassy carbon. Its electrolyte for alkaline media was a 0.1 M KOH aqueous solution. The electrolyte was purged with oxygen for at least 15 min to saturate the liquid solution. In all the measurement processes, for having an oxygen-saturated solution the oxygen gas was pumped into the solution. The

potential scan range was from 1.2 V to 0 V versus RHE in alkaline media. All measured potentials were converted to potential versus RHE according to (Equation 1). The potential of the ring was fixed at 1.2 V versus RHE along with the experiments. The currents generated by the disk (I_d) and by the ring (I_r) were recorded and they were used to calculate the hydrogen peroxide anion produced (Equation 2) and the number of electrons transferred (n) (Equation 3) following the equations:

$$\text{Peroxide} = \frac{200 \cdot \frac{I_r}{N}}{I_d + \frac{I_r}{N}} [\%] \quad (2)$$

$$n = \frac{4 \cdot I_d}{I_d + \frac{I_r}{N}} [\text{nr}] \quad (3)$$

where N is the collection efficiency that was 0.38 as reported by the supplier.

Three parameters are usually used to characterize the ORR electrocatalytic activity: (1) the onset potential (E_{on}), (2) the half-wave potential ($E_{1/2}$), and (3) the limiting current density (j_{lim}). The onset potential was evaluated by recording the potential generated at a current density of 0.1 mA cm^{−2} in a steady-state measurement.⁸⁹ Moreover, the potential where half of the maximum current density in the polarization curve is measured is named half-wave potential.

ACKNOWLEDGMENTS


C.S. would like to thank the support from the Italian Ministry of Education, Universities and Research (Ministero dell'Istruzione, dell'Università e della Ricerca—MIUR) through the “Rita Levi Montalcini 2018” fellowship (Grant

number PGR18MAZLI). The authors also thank the Italian ministry MIUR for funding through the FISIR 2019 project AMPERE (FISIR2019_01294). SAM acknowledges a PhD scholarship on Green Issues from action IV.5 of the PON Research and Innovation 2014-2020 “Education and research for recovery—REACT- EU” program.

CONFLICT OF INTEREST STATEMENT

The authors declare no conflict of interest.

ORCID

Giorgio Tseberlidis  <https://orcid.org/0000-0002-9224-180X>

Enrico Berretti  <https://orcid.org/0000-0001-8200-4301>

Carlo Santoro  <https://orcid.org/0000-0002-0944-4500>

REFERENCES

- Schlapbach L, Züttel A. Hydrogen-storage materials for mobile applications. *Nature*. 2001;414(6861):353-358.
- Atanassov P, Noto VD, McPhail S. From hydrogen manifesto, through green deal and just transition, to clean energy act. *Electrochem Soc Interface*. 2021;30(4):57.
- Kusoglu A. Chalkboard 1-the many colors of hydrogen. *Electrochem Soc Interface*. 2021;30(4):44.
- Hydrogen. Accessed November 8, 2022. https://energy.ec.europa.eu/topics/energy-systems-integration/hydrogen_en
- Santoro C, Lavacchi A, Mustarelli P, et al. What is next in anion-exchange membrane water electrolyzers? *ChemSusChem*. 2022;15(8):e202200027.
- Huang X, Wang Y, Li W, Hou Y. Noble metal-free catalysts for oxygen reduction reaction. *Sci Chin Chem*. 2017;60(12):1494-1507.
- Li Q, Sun S. Recent advances in the organic solution phase synthesis of metal nanoparticles and their electrocatalysis for energy conversion reactions. *Nano Energy*. 2016;29:178-197.
- Zeng M, Li Y. Recent advances in heterogeneous electrocatalysts for the hydrogen evolution reaction. *J Mater Chem A*. 2015;3(29):14942-14962.
- Noori, MdT, Bhowmick GD, Tiwari BR, Ghangrekar MM, Mukhrejee CK. Application of low-cost Cu-Sn bimetal alloy as oxygen reduction reaction catalyst for improving performance of the microbial fuel cell. *MRS Adv*. 2018;3(13):663-668.
- Friebel D, Louie MW, Bajdich M, et al. Identification of highly active Fe sites in (Ni,Fe)OOH for electrocatalytic water splitting. *J Am Chem Soc*. 2015;137(3):1305-1313.
- Critical raw materials. Accessed November 8, 2022. https://single-market-economy.ec.europa.eu/sectors/raw-materials/areas-specific-interest/critical-raw-materials_en
- Zou X, Zhang Y. Noble metal-free hydrogen evolution catalysts for water splitting. *Chem Soc Rev*. 2015;44(15):5148-5180.
- Singh K, Razmjooei F, Yu JS. Active sites and factors influencing them for efficient oxygen reduction reaction in metal-N coordinated pyrolyzed and non-pyrolyzed catalysts: a review. *J Mater Chem A*. 2017;5(38):20095-20119.
- He Y, Liu S, Priest C, Shi Q, Wu G. Atomically dispersed metal-nitrogen-carbon catalysts for fuel cells: advances in catalyst design, electrode performance, and durability improvement. *Chem Soc Rev*. 2020;49(11):3484-3524.
- Artyushkova K, Serov A, Rojas-Carbonell S, Atanassov P. Chemistry of multitudinous active sites for oxygen reduction reaction in transition metal-nitrogen-carbon electrocatalysts. *J Phys Chem C*. 2015;119(46):25917-25928.
- Chen MX, Tong L, Liang HW. Understanding the catalytic sites of metal-nitrogen-carbon oxygen reduction electrocatalysts. *Chem Eur J*. 2021;27(1):145-157.
- Sultan S, Tiwari JN, Singh AN, et al. Single atoms and clusters based nanomaterials for hydrogen evolution, oxygen evolution reactions, and full water splitting. *Adv Energy Mater*. 2019;9(22):1900624.
- Zhang Q, Guan J. Atomically dispersed catalysts for hydrogen/oxygen evolution reactions and overall water splitting. *J Power Sources*. 2020;471:228446.
- Santoro C, Bollella P, Erable B, Atanassov P, Pant D. Oxygen reduction reaction electrocatalysis in neutral media for bioelectrochemical systems. *Nat Catal*. 2022;5(6):473-484.
- Meng Y, Huang X, Lin H, Zhang P, Gao Q, Li W. Carbon-based nanomaterials as sustainable noble-metal-free electrocatalysts. *Front Chem*. 2019;7:759.
- Baghban A, Habibzadeh S, Zokaee Ashtiani F. On the evaluation of hydrogen evolution reaction performance of metal-nitrogen-doped carbon electrocatalysts using machine learning technique. *Sci Rep*. 2021;11(1):21911.
- Sgarbi R, Kumar K, Jaouen F, Zitolo A, Ticianelli EA, Maillard F. Oxygen reduction reaction mechanism and kinetics on M-NxCy and M@N-C active sites present in model M-N-C catalysts under alkaline and acidic conditions. *J Solid State Electrochem*. 2021;25(1):45-56.
- Du L, Shao Y, Sun J, Yin G, Liu J, Wang Y. Advanced catalyst supports for PEM fuel cell cathodes. *Nano Energy*. 2016;29:314-322.
- Du L, Zhang G, Liu X, et al. Biomass-derived nonprecious metal catalysts for oxygen reduction reaction: the demand-oriented engineering of active sites and structures. *Carbon Energy*. 2020;2(4):561-581.
- Yan D, Li Y, Huo J, Chen R, Dai L, Wang S. Defect chemistry of nonprecious-metal electrocatalysts for oxygen reactions. *Adv Mater*. 2017;29(48):1606459.
- Li J, Sougrati MT, Zitolo A, et al. Identification of durable and non-durable FeNx sites in Fe-N-C materials for proton exchange membrane fuel cells. *Nat Catal*. 2021;4(1):10-19.
- Wang HY, Weng CC, Yuan ZY. Insights into efficient transition metal-nitrogen/carbon oxygen reduction electrocatalysts. *J Energy Chem*. 2021;56:470-485.
- de Oliveira MAC, Ficca VCA, Gokhale R, et al. Iron(II) phthalocyanine (FePc) over carbon support for oxygen reduction reaction electrocatalysts operating in alkaline electrolyte. *J Solid State Electrochem*. 2021;25(1):93-104.
- Kimura M, Kuroda T, Ohta K, Hanabusa K, Shirai H, Kobayashi N. Self-organization of hydrogen-bonded optically active phthalocyanine dimers. *Langmuir*. 2003;19(11):4825-4830.
- Abarca G, Viera M, Aliaga C, et al. In search of the most active MN4 catalyst for the oxygen reduction reaction. The case of perfluorinated Fe phthalocyanine. *J Mater Chem A*. 2019;7(43):24776-24783.

31. Wang Q, Guo R, Wang Z, et al. Progress in carbon-based electrocatalyst derived from biomass for the hydrogen evolution reaction. *Fuel*. 2021;293:120440.
32. Zhu J, Hu L, Zhao P, Lee LYS, Wong KY. Recent advances in electrocatalytic hydrogen evolution using nanoparticles. *Chem Rev*. 2020;120(2):851-918.
33. Yuan YJ, Tu JR, Lu HW, Yu ZT, Fan XX, Zou ZG. Neutral nickel(ii) phthalocyanine as a stable catalyst for visible-light-driven hydrogen evolution from water. *Dalton Trans*. 2016;45(4):1359-1363.
34. Satyawali SSY. Enzymatic electrosynthesis: an overview on the progress in enzyme- electrodes for the production of electricity, fuels and chemicals. *J Microb Biochem Technol*. 2013;S6:1-20.
35. Daniel G, Kosmala T, Dalconi MC, et al. Upcycling of polyurethane into iron-nitrogen-carbon electrocatalysts active for oxygen reduction reaction. *Electrochim Acta*. 2020;362:137200.
36. Borghesi M, Lehtonen J, Liu L, Rojas OJ. Advanced biomass-derived electrocatalysts for the oxygen reduction reaction. *Adv Mater*. 2018;30(24):1703691.
37. Daniel G, Foltran E, Brandiele R, et al. Platinum-free electrocatalysts for oxygen reduction reaction: Fe-N_x modified mesoporous carbon prepared from biosources. *J Power Sources*. 2018;402:434-446.
38. Muhyuddin M, Mustarelli P, Santoro C. Recent advances in waste plastic transformation into valuable platinum-group metal-free electrocatalysts for oxygen reduction reaction. *ChemSusChem*. 2021;14(18):3785-3800.
39. Muhyuddin M, Zocche N, Lorenzi R, et al. Valorization of the inedible pistachio shells into nanoscale transition metal and nitrogen codoped carbon-based electrocatalysts for hydrogen evolution reaction and oxygen reduction reaction. *Mater Renew Sustain Energy*. 2022;11(2):131-141.
40. Ouyang C, Wang X. Recent progress in pyrolyzed carbon materials as electrocatalysts for the oxygen reduction reaction. *Inorg Chem Front*. 2020;7(1):28-36.
41. Singh A, Sharma R, Pant D, Malaviya P. Engineered algal biochar for contaminant remediation and electrochemical applications. *Sci Total Environ*. 2021;774:145676.
42. Zago S, Bartoli M, Muhyuddin M, et al. Engineered biochar derived from pyrolyzed waste tea as a carbon support for Fe-N-C electrocatalysts for the oxygen reduction reaction. *Electrochim Acta*. 2022;412:140128.
43. Huggins T, Wang H, Kearns J, Jenkins P, Ren ZJ. Biochar as a sustainable electrode material for electricity production in microbial fuel cells. *Bioresour Technol*. 2014;157:114-119.
44. Yuan H, Deng L, Qi Y, Kobayashi N, Tang J. Nonactivated and activated biochar derived from bananas as alternative cathode catalyst in microbial fuel cells. *Sci World J*. 2014;2014:e832850.
45. Chen H, Huang X. Overview of litchi production in the world with specific reference to China. *Acta Hort*. 2014;1029:25-33.
46. Zhao L, Wang K, Wang K, Zhu J, Hu Z. Nutrient components, health benefits, and safety of litchi (*Litchi chinensis* Sonn.): a review. *Compr Rev Food Sci Food Saf*. 2020;19(4):2139-2163.
47. Sarni-Manchado P, Le Roux E, Le Guernevé C, Lozano Y, Cheynier V. Phenolic composition of litchi fruit pericarp. *J Agric Food Chem*. 2000;48(12):5995-6002.
48. Ferrari AC, Robertson J. Interpretation of Raman spectra of disordered and amorphous carbon. *Phys Rev B*. 2000;61(20):14095-14107.
49. Saenger KL, Tsang JC, Bol AA, Chu JO, Grill A, Lavoie C. In situ X-ray diffraction study of graphitic carbon formed during heating and cooling of amorphous-C/Ni bilayers. *Appl Phys Lett*. 2010;96(15):153105.
50. Hu M, Reboul J, Furukawa S, et al. Direct carbonization of Al-based porous coordination polymer for synthesis of nanoporous carbon. *J Am Chem Soc*. 2012;134(6):2864-2867.
51. Bozovic N, Bozovic I, Misewich J. X-ray nanocrystallography of individual carbon nanotubes. *Nano Lett*. 2008;8(12):4477-4482.
52. Graf D, Molitor F, Ensslin K, et al. Spatially resolved Raman spectroscopy of single- and few-layer graphene. *Nano Lett*. 2007;7(2):238-242.
53. Wang B, Li X, Luo B, et al. Pyrolyzed bacterial cellulose: a versatile support for lithium ion battery anode materials. *Small*. 2013;9(14):2399-2404.
54. Malard LM, Pimenta MA, Dresselhaus G, Dresselhaus MS. Raman spectroscopy in graphene. *Phys Rep*. 2009;473(5):51-87.
55. Cançado LG, Jorio A, Ferreira EHM, et al. Quantifying defects in graphene via Raman spectroscopy at different excitation energies. *Nano Lett*. 2011;11(8):3190-3196.
56. Ferrari AC. Raman spectroscopy of graphene and graphite: disorder, electron-phonon coupling, doping and nonadiabatic effects. *Solid State Commun*. 2007;143(1):47-57.
57. Xu X, Shi C, Li Q, Chen R, Chen T. Fe-N-doped carbon foam nanosheets with embedded Fe₂O₃ nanoparticles for highly efficient oxygen reduction in both alkaline and acidic media. *RSC Adv*. 2017;7(24):14382-14388.
58. Yan X, Jia Y, Yao X. Defects on carbons for electrocatalytic oxygen reduction. *Chem Soc Rev*. 2018;47(20):7628-7658.
59. Yang L, Shui J, Du L, et al. Carbon-based metal-free ORR electrocatalysts for fuel cells: past, present, and future. *Adv Mater*. 2019;31(13):1804799.
60. Zhang L, Jia Y, Yan X, Yao X. Activity origins in nanocarbons for the electrocatalytic hydrogen evolution reaction. *Small*. 2018;14(26):1800235.
61. Ferrari AC, Meyer JC, Scardaci V, et al. Raman spectrum of graphene and graphene layers. *Phys Rev Lett*. 2006;97(18):187401.
62. Matsoso BJ, Ranganathan KK, Mutuma B, Lerotholi T, Jones GJ, Coville N. Time-dependent evolution of the nitrogen configurations in N-doped graphene films. *RSC Adv*. 2016;6(108):106914-106920.
63. Sundar Rajan A, Sampath S, Kumar Shukla A. An in situ carbon-grafted alkaline iron electrode for iron-based accumulators. *Energy Environ Sci*. 2014;7(3):1110-1116.
64. Yang H, Shang L, Zhang Q, et al. A universal ligand mediated method for large scale synthesis of transition metal single atom catalysts. *Nat Commun*. 2019;10(1):4585.
65. Sun S, Zhang G, Gauquelin N, et al. Single-atom catalysis using Pt/graphene achieved through atomic layer deposition. *Sci Rep*. 2013;3(1):1775.
66. Lo Vecchio C, Aricò AS, Baglio V. Application of low-cost Me-N-C (Me = Fe or Co) electrocatalysts derived from EDTA in direct methanol fuel cells (DMFCs). *Materials*. 2018;11(7):1193.
67. Lo Vecchio C, Aricò AS, Monforte G, Baglio V. EDTA-derived CoNC and FeNC electro-catalysts for the oxygen reduction reaction in acid environment. *Renew Energy*. 2018;120:342-349.
68. Chen S, Bi F, Xiang K, et al. Reactive template-derived CoFe/N-doped carbon nanosheets as highly efficient electrocatalysts toward oxygen reduction, oxygen evolution, and hydrogen evolution. *ACS Sustain Chem Eng*. 2019;7(18):15278-15288.

69. Mercado R, Wahl C, En Lu J, et al. Nitrogen-doped porous carbon cages for electrocatalytic reduction of oxygen: enhanced performance with iron and cobalt dual metal centers. *ChemCatChem*. 2020;12(12):3230-3239.
70. Song XW, Zhang S, Zhong H, et al. FeCo nanoalloys embedded in nitrogen-doped carbon nanosheets/bamboo-like carbon nanotubes for the oxygen reduction reaction. *Inorg Chem Front*. 2021;8(1):109-121.
71. Liu SH, Kuo HC. Core-shell FeCo N-doped biocarbons as stable electrocatalysts for oxygen reduction reaction in fuel cells. *Int J Energy Res*. 2021;45(6):8285-8295.
72. Gokhale R, Chen Y, Serov A, Artyushkova K, Atanassov P. Direct synthesis of platinum group metal-free Fe-N-C catalyst for oxygen reduction reaction in alkaline media. *Electrochem Commun*. 2016;72:140-143.
73. Zhou Y, Zhang Y, Xu X, et al. Bimetallic metal-organic framework derived metal-carbon hybrid for efficient reversible oxygen electrocatalysis. *Front Chem*. 2019;7:747.
74. Alegre C, Busacca C, Di Blasi A, et al. Electrocatalysis of oxygen on bifunctional nickel-cobaltite spinel. *ChemElectroChem*. 2020;7(1):124-130.
75. Serov A, Artyushkova K, Andersen NI, Stariha S, Atanassov P. Original mechanochemical synthesis of non-platinum group metals oxygen reduction reaction catalysts assisted by sacrificial support method. *Electrochim Acta*. 2015;179:154-160.
76. Ramaswamy N, Mukerjee S. Influence of inner- and outer-sphere electron transfer mechanisms during electrocatalysis of oxygen reduction in alkaline media. *J Phys Chem C*. 2011;115(36):18015-18026.
77. Ding J, Yang H, Zhang S, et al. Advances in the electrocatalytic hydrogen evolution reaction by metal nanoclusters-based materials. *Small*. 2022;18(52):2204524.
78. Muhyuddin M, Friedman A, Poli F, et al. Lignin-derived bimetallic platinum group metal-free oxygen reduction reaction electrocatalysts for acid and alkaline fuel cells. *J Power Sources*. 2023;556:232416.
79. Mirshokraee SA, Muhyuddin M, Morina R, et al. Upcycling of waste lithium-cobalt-oxide from spent batteries into electrocatalysts for hydrogen evolution reaction and oxygen reduction reaction: a strategy to turn the trash into treasure. *J Power Sources*. 2023;557:232571.
80. Rojas-Carbonell S, Santoro C, Serov A, Atanassov P. Transition metal-nitrogen-carbon catalysts for oxygen reduction reaction in neutral electrolyte. *Electrochem Commun*. 2017;75:38-42.
81. Osmieri L, Monteverde Videla AHA, Ocón P, Specchia S. Kinetics of oxygen electroreduction on Me-N-C (Me = Fe, Co, Cu) catalysts in acidic medium: insights on the effect of the transition metal. *J Phys Chem C*. 2017;121(33):17796-17817.
82. Serov A, Robson MH, Smolnik M, Atanassov P. Tri-metallic transition metal-nitrogen-carbon catalysts derived by sacrificial support method synthesis. *Electrochim Acta*. 2013;109:433-439.
83. Serov A, Robson MH, Smolnik M, Atanassov P. Templated bimetallic non-PGM catalysts for oxygen reduction. *Electrochim Acta*. 2012;80:213-218.
84. Galiote NA, Oliveira FER, Lima FHB. FeCo-N-C oxygen reduction electrocatalysts: activity of the different compounds produced during the synthesis via pyrolysis. *Appl Catal B Environ*. 2019;253:300-308.
85. Muhyuddin M, Testa D, Lorenzi R, et al. Iron-based electrocatalysts derived from scrap tires for oxygen reduction reaction: evolution of synthesis-structure-performance relationship in acidic, neutral and alkaline media. *Electrochim Acta*. 2022;433:141254.
86. Lv Y, Zhang F, Dou Y, et al. A comprehensive study on KOH activation of ordered mesoporous carbons and their supercapacitor application. *J Mater Chem*. 2012;22(1):93-99.
87. Muhyuddin M, Filippi J, Zoia L, et al. Waste face surgical mask transformation into crude oil and nanostructured electrocatalysts for fuel cells and electrolyzers. *ChemSusChem*. 2022;15(2):e202102351.
88. Garsany Y, Baturina OA, Swider-Lyons KE, Kocha SS. Experimental methods for quantifying the activity of platinum electrocatalysts for the oxygen reduction reaction. *Anal Chem*. 2010;82(15):6321-6328.
89. Wu G, More KL, Johnston CM, Zelenay P. High-performance electrocatalysts for oxygen reduction derived from polyaniline, iron, and cobalt. *Science*. 2011;332(6028):443-447.

SUPPORTING INFORMATION

Additional supporting information can be found online in the Supporting Information section at the end of this article.

How to cite this article: Mirshokraee SA, Muhyuddin M, Lorenzi R, et al. Litchi-derived platinum group metal-free electrocatalysts for oxygen reduction reaction and hydrogen evolution reaction in alkaline media. *SusMat*. 2023;1-15.
<https://doi.org/10.1002/sus2.121>